JOURNAL OF COASTAL AND HYDRAULIC STRUCTURES

Wave environment analysis at Norwegian harbours for land-based aquaculture facilities using a combined phase-averaging and phase-resolving numerical modelling approach

Knut Reidulff[1], Weizhi Wang[2], Arun Kamath[2], and Hans Bihs[2]

Abstract

Numerical wave modelling of Norwegian coastal areas is challenging due to the drastically varying bathymetry, irregular coastline, and large domains of interest. The widely used phase-averaging models are limited by such bathymetric and topographic conditions. Phase-resolving models provide higher accuracy regarding strong nonlinear wave transformations with the trade-off of a higher computational cost. This study provides a combined phase-averaging and phase-resolving modelling approach to analyse the wave conditions for on-shore aquaculture facilities at the site candidates Fiskenes and Breivik, Andøya, Norway. The phase-averaging spectral model SWAN is used for the offshore sea state analysis based on the offshore hind-cast data. The analysis is performed on cascade nested grids, with increasing accuracy closer to the proposed harbour locations. A novel interpolation algorithm is proposed to provide comprehensive sea state information with every offshore wave directions without requiring additional simulations. The critical wave conditions are identified from SWAN and used as input to the open-source phase-resolving fully nonlinear potential flow model REEF3D::FNPF. Four scenarios are investigated and densely spaced wave gauges in the entire computational domain provide the distribution of significant wave height. The combined and cascade simulation approach helps to achieve a balance between computational efficiency and accuracy for large-scale marine environment assessment. The results show detailed wave statistics in the entire area of relevance near both harbours and provide a quantitative reference for both the site choice and the harbour assessment.

Keywords:

[1]knut.reidulff@vedal.no; Vedal AS, Oslo, Norway
[2]weizhi.wang@ntnu.no, arun.kamath@ntnu.no, hans.bihs@ntnu.no; Norwegian University of Science and Technology NTNU, Trondheim, Norway

1 Introduction

Land-based fish farming has roots back in the 60s but has never been a commercially viable option compared to its net-based counterpart at sea (Fjørtoft and Fondevik, 2020). Technological progress, however, such as developments in recirculating aquaculture systems (RAS), have created profitable opportunities for land-based fish farming (Fjørtoft and Fondevik, 2020). In addition to the technical readiness, the concern over environmental impacts from the waterborn net-based fish farms has also made the land-based alternative more attractive. It is planned to produce 10 000 metric tonnes of farmed salmon at Andøya (Andfjord Salmon, 2021) with potential further expansion to additional locations including Fiskenes, Breivik, and Kvalnes, as seen in Fig. 1.

Andøya is located in the Norwegian archipelago Lofoten - Vesterålen and has unique advantages for Atlantic salmon farming. The inflow of continuous oxygen-rich seawater from the Gulf stream, see Fig. 1, provides stable sea-water
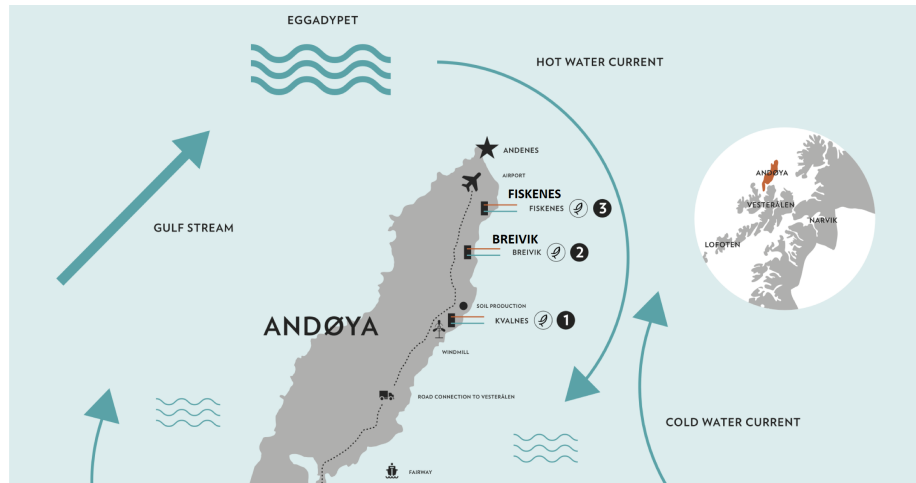
Figure 1: Possible fish farming locations and overview of Andøya (Andfjord Salmon, 2021)

temperatures which are excellent for salmon growth and health in the shore-based tanks. Although the facility will be based onshore, the construction of a breakwater is necessary to protect the farming facility in addition to providing shelter and safe harbouring for ships docking to provide food for the salmon. The concept design of the harbour facility for the on-shore aquaculture is seen in Fig. 2. Although Andøya has several advantages for farming salmon, its coastal area is subject to strong winds and severe wave conditions. In addition, the drastically changing bathymetry and irregular coastline make wave modelling a challenging endeavour.

Figure 2: Fiskenes Harbor concept (NRK, 2022)

Phase-averaging models, such as spectral models, are the most common wave models used by consulting firms today. Spectral models such as SWAN (Booij et al., 1999) and STWAVE (Massey et al., 2011) are two-dimensional and use a multi-directional wave spectrum to represent the wave state in the simulated domain (Ardhuin and Roland, 2013). For some locations, such as the coastal areas of western Europe, and in deep and intermediate waters with small variations in bathymetry, spectral models such as SWAN and STWAVE have proven to provide reliable results. In addition, it is significantly easier to add the influence from winds and currents into a simulation as source terms in the governing equation of a spectral wave model. Regardless of the computational efficiency and the possible inclusion of wind and currents, spectral models have an inherent weakness in coastal areas with strongly varying bathymetry and irregular coastlines(Wang, 2020). Norway's coast is known for its large variations in bathymetry, islands, and jagged coastline making spectral models such as SWAN less suitable. The use of spectral models at inappropriate locations may lead to incorrect estimations of the sea-state and thus incorrect design basis for coastal structures.

An alternative is therefore needed to ensure sufficient accuracy in the wave modelling results for coastal regions in Norway. Phase-resolving models provide an attractive alternative to the commonly used phase-averaging models. Unlike phase-averaging spectral models, phase-resolving models explicitly reproduce the free surface and the velocity field which enables the representation of the quick variations in wave parameters and nonlinear wave transformations (Wang, 2020). The downside of phase-resolving models, however, is that the increased accuracy comes with a relatively high computational cost. As a result, they usually require high-performance computing (HPC) facilities to

conduct an analysis in a reasonable time. The computational fluid dynamics (CFD) models such as OpenFOAM (OpenFOAM (2019)), ReFRESCO(Vaz et al. (2009)), ANSYS-Fluent (OpenFOAM (2019)), Star CCM+ (Siemens (2019)) and REEF3D::CFD (Bihs et al. (2016b)) provide the most detailed flow field information but require significant computational resources and simulation time. This makes it less practical for large-domain harbour-scale analysis. Depth-averaging enables the shallow water equation (SWE) based models such as Boussinesq-type models(Madsen et al., 1991; Nwogu, 1993; Shi et al., 2012; Madsen et al., 2002) multi-layer models (Stelling and Duinmeijer, 2003; Zijlema and Stelling, 2005, 2008; Zijlema et al., 2011) and quadratic hydrodynamic pressure models (Jeschke et al., 2017; Wang et al., 2020b) significantly improve the computational efficiency in comparison to CFD models. However, the depth-averaging technique is most suitable for shallow to intermediate water depth. The computational stability of Boussinesq-type models, the computational efficiency of the multi-layer models and the applicability of quadratic hydrodynamic pressure models deteriorate in deep water regions. Alternatively, the potential flow models based on boundary element method (BEM) (Grilli et al., 1994, 2020), high-order spectrum method (HOS) (Ducrozet et al., 2012; Bonnefoy et al., 2006a,b; Raoult et al., 2016; Yates and Benoit, 2015) and finite difference method (FDM) (Li and Fleming, 1997; Bingham and Zhang, 2007; Engsig-Karup et al., 2009) are not limited by water depth conditions. However, the treatment of breaking waves, varying bathymetry and irregular coastlines are some of the main challenges. Various techniques have been developed to tackle these challenges while keeping computational efficiency and stability. Wang et al. (2022) combined the proven breaking algorithms and introduced the novel level-set method (LSM)-based coastline algorithm in the σ-grid based fully-nonlinear potential flow model REEF3D::FNPF (Bihs et al., 2020a). As a result, the model showed universal efficient coastline capturing capability and robust wave transformation representation with a computational efficiency in the order of 1000 faster than CFD models (Wang et al., 2020a).

The phase-averaging models and the phase-resolving models have complementary advantages. The computational efficiency of the phase-averaging models is suitable for the offshore wave condition assessment. This enables the analysis of many scenarios and the identification of critical situations. The critical events can be resolved in detail in the phase-resolving models, enabling near-site sea state analysis with much-improved accuracy, especially for non-linear wave transformations such as diffraction.

In this work, we employ both the phase-averaging model SWAN and the phase-resolving model REEF3D::FNPF in a combined approach to optimise the balance of efficiency and accuracy in the marine environment assessment of the harbour design for land-based aquaculture. SWAN is computationally more efficient and is able to include wind forcing for wave generation and thus can be used for large-domain offshore sea-state evaluation and provides input boundary for the modelling of coastal wave transformations in REEF3D::FNPF. In addition, in the combined approach, a complete cascade procedure is developed for the coastal wave analysis using only offshore hind-cast data. The nested grid is used in SWAN for refined accuracy near the harbour area. A novel interpolation algorithm is used to obtain sea states in between simulated scenarios with good accuracy. This enables a comprehensive overview of the offshore conditions for the identification of critical events. The identified critical and representative wave conditions are simulated in REEF3D::FNPF, where the time domain results are interpreted as a distribution of significant wave height in the entire simulation domain, thanks to the flexible and densely spaced wave gauges in the numerical wave tank. The study aims to provide an industry-application-ready procedure using open-source models in an accurate and efficient manner.

2 Input data and numerical models

2.1 Hindcast data

The offshore wave data is accessed using the WAM10 dataset (Reistad et al., 2009). The closest measuring point in the WAM10 data set is N70.73°/ E19.92°, about 200 kilometers NE of Andenes. The WAM10 hind-cast data is calculated using several measurements from 1957 to 2015 in order to predict extreme values for waves and wind. An overview of the return period for offshore waves can be seen in Fig. 3. According to the Norwegian regulations on technical requirements for construction works, TEK17 §7-2 (Norwegian Building Authority, 2017), the harbour and breakwater must be constructed to cope with a 200-year return period event. Therefore, this wave analysis is conducted with hind-cast data for a 200-year return period, as summarised in Table 1.
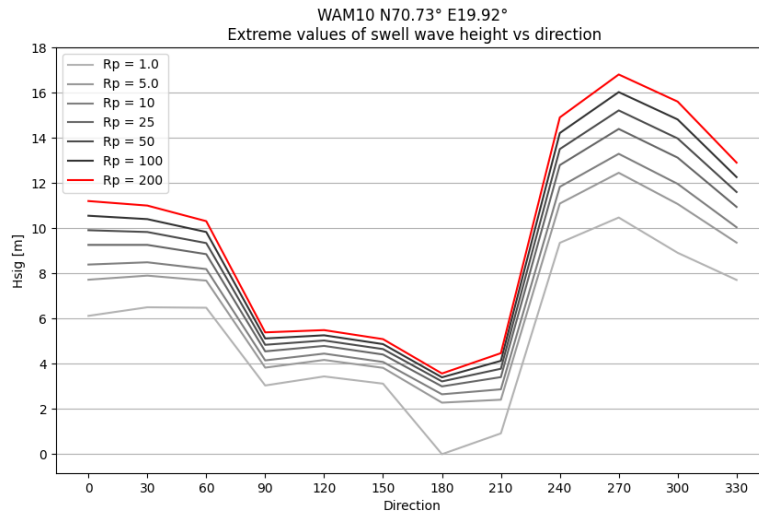
Reidulff, K. et. al.

Figure 3: Overview of hind-cast data from WAM10 (Reistad et al., 2009). Rp is the return period

Direction	Significant wave height, Hs [m]	Peak period, Tp [s]
240	14.9	16
270	16.8	18
300	15.6	17
330	12.9	15
0	11.2	14
30	11.0	14
60	10.3	14
90	5.39	12

Table 1: Wave parameters for a 200 year return period

2.2 SWAN

The spectral analysis is conducted in Simulating WAves Nearshore (SWAN) developed at TU Delft (Booij et al., 1999). In this section, a short overview of the numerical methods employed in SWAN is discussed.

SWAN calculates the development of the sea state by the means of action density $N(f_\sigma, \theta)$. Action density is defined as the variance density $E(f_\sigma, \theta)$ divided by the relative frequency f_σ.

$$N(f_\sigma, \theta) = \frac{E(f_\sigma, \theta)}{f_\sigma} \tag{1}$$

where f_σ is the relative frequency and θ is the wave direction.

The evolution of the wave spectrum is described by an energy balance approach of the wave energy density. The balance of wave energy is defined in cells distributed in a two-dimensional grid. For all cells, of size $\delta x \delta y$, and over a time interval δt the following must be satisfied:

$$Change\ of\ energy = Net\ import\ of\ energy + Net\ local\ dissipation \tag{2}$$

By applying the principle of the energy balance approach we get the following expression for deep water in the absence of currents:

$$\frac{\partial}{\partial t} E + \frac{\partial}{\partial x} (c_x E) + \frac{\partial}{\partial y} (c_y E) = S(f_\sigma, \theta; x, y, t) \tag{3}$$

where c_x and c_y are components of the group velocity in the x and y direction, and $S(f_\sigma, \theta; x, y, t)$ is the source term that represents the effects of generation and dissipation.

If the energy balance equation, eq. 2, is applied to coastal waters we obtain the following:

$$\frac{\partial}{\partial t} N + \frac{\partial}{\partial x} (c_x N) + \frac{\partial}{\partial y} (c_y N) + \frac{\partial}{\partial f_\sigma} (c_{f_\sigma} N) + \frac{\partial}{\partial \theta} (c_\theta N) = \frac{S(f_\sigma, \theta; x, y, t)}{f_\sigma} \tag{4}$$

where,

$\frac{\partial}{\partial t} N$ is the rate of change of action

$\frac{\partial}{\partial x} (c_x N) + \frac{\partial}{\partial y} (c_y N)$ represents the propagation of wave action in the 2D plane

$\frac{\partial}{\partial f_\sigma} (c_{f_\sigma} N)$ represents the frequency shift

$\frac{\partial}{\partial \theta} (c_\theta N)$ represents the refraction effects induced by currents and depth

$S(f_\sigma, \theta)$ represents the effects from generation, dissipation and nonlinear wave-wave interactions. Specifically, these effects include:

S_{inp} - generation due to wind input

S_{brk} - depth induced wave breaking

S_{frc} - bottom friction

S_{wcp} - whitecapping

S_{nl3} - triad wave-wave interactions

S_{nl4} - quadruplet wave-wave interactions

2.3 REEF3D::FNPF

REEF3D is an open-source hydrodynamic framework under continuous development covering multi-scales and multi-physics (Bihs et al., 2016a; Alagan Chella et al., 2019; Ahmad et al., 2020; Martin et al., 2020). Among its submodels, the fully nonlinear potential flow model REEF3D::FNPF (Bihs et al., 2020b; Wang et al., 2021, 2022) is presented in this study. In REEF3D::FNPF, the governing equation is the Laplace equation:

$$\frac{\partial^2 \Phi}{\partial x^2} + \frac{\partial^2 \Phi}{\partial y^2} + \frac{\partial^2 \Phi}{\partial z^2} = 0 \tag{5}$$

The Laplace equation and boundary conditions are solved in a σ-coordinate system. Φ is the velocity potential in the σ-coordinate system. The σ-coordinate system follows the bathymetry and the free surface so that the water depth variation is intrinsically represented. The conversion from a Cartesian grid system to the σ-grid is defined as follows:

$$\sigma = \frac{z + h(\mathbf{x})}{\eta(\mathbf{x}, t) + h(\mathbf{x})} \tag{6}$$

$h(\mathbf{x})$ and $\eta(\mathbf{x}, t)$ are the local water depth and free surface elevation level in the Cartesian grid system. Near the surface, a more refined mesh is required to ensure sufficient accuracy. In the model, the vertical coordinates are defined from the following stretching function such that the grid becomes denser toward the free-surface:

$$\sigma_i = \frac{\sinh(-\alpha) - \sinh\left(\alpha\left(\frac{i}{N_z} - 1\right)\right)}{\sinh(-\alpha)}, \tag{7}$$

Where α is the stretching factor, N_z is the number of cells in the vertical direction. The velocity potential ϕ after the σ-grid transformation is denoted as Φ. The velocity potential can only be solved with the closure of the boundary conditions. These boundary conditions in the σ-grid are presented at the free surface at $\sigma = 1$ and the bottom at $\sigma = 0$.

$$
\begin{aligned}
&\Phi = \widetilde{\phi} && ,\sigma = 1 \\
&\frac{\partial^2 \Phi}{\partial x^2} + \frac{\partial^2 \Phi}{\partial y^2} + \left(\frac{\partial^2 \sigma}{\partial x^2} + \frac{\partial^2 \sigma}{\partial y^2} \right) \frac{\partial \Phi}{\partial \sigma} + 2 \left(\frac{\partial \sigma}{\partial x} \frac{\partial}{\partial x} \left(\frac{\partial \Phi}{\partial \sigma} \right) + \right. && \\
&\frac{\partial \sigma}{\partial y} \frac{\partial}{\partial y} \left(\frac{\partial \Phi}{\partial \sigma} \right) + \left(\left(\frac{\partial \sigma}{\partial x} \right)^2 + \left(\frac{\partial \sigma}{\partial y} \right)^2 + \left(\frac{\partial \sigma}{\partial z} \right)^2 \right) \frac{\partial^2 \Phi}{\partial \sigma^2} = 0 && ,0 \le \sigma < 1; \\
&\left(\frac{\partial \sigma}{\partial z} + \frac{\partial h}{\partial x} \frac{\partial \sigma}{\partial x} + \frac{\partial h}{\partial y} \frac{\partial \sigma}{\partial y} \right) \frac{\partial \Phi}{\partial \sigma} + \frac{\partial h}{\partial x} \frac{\partial \Phi}{\partial x} + \frac{\partial h}{\partial y} \frac{\partial \Phi}{\partial y} = 0 && ,\sigma = 0
\end{aligned}
\tag{8}
$$

$\widetilde{\phi}$ is the velocity potential at the free surface. After the velocity potential Φ is solved in the σ-grid one may solve for the velocities:

$$
u\left(\mathbf{x}, z\right) = \frac{\partial \Phi\left(\mathbf{x}, z\right)}{\partial x} = \frac{\partial \Phi\left(\mathbf{x}, \sigma\right)}{\partial x} + \frac{\partial \sigma}{\partial x} \frac{\partial \Phi\left(\mathbf{x}, \sigma\right)}{\partial \sigma},
\tag{9}
$$

$$
v\left(\mathbf{x}, z\right) = \frac{\partial \Phi\left(\mathbf{x}, z\right)}{\partial y} = \frac{\partial \Phi\left(\mathbf{x}, \sigma\right)}{\partial y} + \frac{\partial \sigma}{\partial y} \frac{\partial \Phi\left(\mathbf{x}, \sigma\right)}{\partial \sigma},
\tag{10}
$$

$$
w\left(\mathbf{x}, z\right) = \frac{\partial \sigma}{\partial z} \frac{\partial \Phi\left(\mathbf{x}, \sigma\right)}{\partial \sigma}.
\tag{11}
$$

The spatial discretisation of the gradient terms of the free-surface boundary conditions, Eqn. 8, is conducted with the use of the 5th-order weighted essentially non-oscillatory (WENO) scheme (Jiang and Shu, 1996). The WENO stencil has three essentially non-oscillatory (ENO) stencils based on smoothness indicators IS ((Jiang and Shu, 1996)). The scheme is designed to ensure that the stencils with the highest smoothness contributes the most to gradient term and thus enables the scheme to handle large gradients with good accuracy.

The time treatment is based on a 3rd-order accurate total variation diminishing (TVD) Runge-Kutta scheme (Shu and Osher, 1988). For increased accuracy and efficiency of the solver, adaptive time stepping is implemented with constant time factor is controlled with the Courant-Friedrichs-Lewy (CFL) condition.

For the simulations conducted in this study, the Laplace equation is discretised using second-order central differences using a parallelised geometric multi-grid preconditioned conjugate gradient solver provided by Hypre (van der Vorst, 1992).

2.3.1 Wave generation and absorption

In this study, the waves are generated using the relaxation method, where the wave generation takes place in a relaxation zone of approximately one wavelength with the peak period. In the relaxation zone, the velocity potential Φ and the free surface η are gradually increased from the computational values to the values obtained from wave theory 13. At the outlet boundary of the domain, the waves need to be absorbed using the relaxation method such that reflections will not influence results.

$$
\Phi(\widetilde{x})_{\text{relaxed}} = \Gamma(\widetilde{x}) \Phi_{\text{analytical}} + (1 - \Gamma(\widetilde{x})) \Phi_{\text{computational}},
\tag{12}
$$

$$
\eta(\widetilde{x})_{\text{relaxed}} = \Gamma(\widetilde{x}) \eta_{\text{analytical}} + (1 - \Gamma(\widetilde{x})) \eta_{\text{computational}},
\tag{13}
$$

where the relaxation function in (Jacobsen et al., 2012) is used:

$$
\Gamma(\widetilde{x}) = 1 - \frac{e^{\left(\widetilde{x}^{3.5}\right)} - 1}{e - 1} \text{ for } \widetilde{x} \in [0; 1]
\tag{14}
$$

The coordinate $\widetilde{x}$ is scaled to the length of the relaxation zones (one wavelength at inlet, two at outlet).

2.3.2 Breaking wave algorithm

REEF3D::FNPF represents the free surface with a single value. An overturning wave needs to be represented with several values of the free surface and thus the model is not suitable to resolve plunging breaking wave geometry as in computational fluid dynamics (CFD) (Wang, 2020). Although overturning plunging breaking waves cannot be geometrically represented, it is still important to include the energy dissipation that occurs with breaking waves.

With an accurate breaking wave algorithm, accurate detection and dissipation may be simulated. In shallow water, the detection of a breaking wave occurs when the vertical velocity of the free surface exceed a fraction of the water celerity.

$$\frac{\partial \eta}{\partial t} \geq \alpha_s \sqrt{gh} \tag{15}$$

$\alpha_s = 0.6$ works well with most waves (Smit et al., 2013).

Deepwater steepness-induced breaking is detected with the following steepness criterion:

$$\frac{\partial \eta}{\partial x_i} \geq \beta \tag{16}$$

After wave breaking is detected, the energy dissipation from the breaking wave process must be represented. There are two main methods for breaking wave energy dissipation, the geometric filtering algorithm (Jensen et al., 1999) or by the introduction of a local viscous dampening term for the free-surface boundary condition around the breaking region (Baquet et al., 2017). A combination of the two methods may be used for complex breaking conditions for more accurate results. For the viscous dampening method, the free surface boundary condition becomes:

$$
\begin{aligned}
\frac{\partial \eta}{\partial t} &= -\frac{\partial \eta}{\partial x}\frac{\partial \widetilde{\phi}}{\partial x} - \frac{\partial \eta}{\partial y}\frac{\partial \widetilde{\phi}}{\partial y} + \widetilde{w}\left(1 + \left(\frac{\partial \eta}{\partial x}\right)^2 + \left(\frac{\partial \eta}{\partial y}\right)^2\right) + \nu_b\left(\frac{\partial^2 \eta}{\partial x^2} + \frac{\partial^2 \eta}{\partial y^2}\right), \\
\frac{\partial \widetilde{\phi}}{\partial t} &= -\frac{1}{2}\left(\left(\frac{\partial \widetilde{\phi}}{\partial x}\right)^2 + \left(\frac{\partial \widetilde{\phi}}{\partial y}\right)^2 - \widetilde{w}^2\left(1 + \left(\frac{\partial \eta}{\partial x}\right)^2 + \left(\frac{\partial \eta}{\partial y}\right)^2\right)\right) - g\eta + \nu_b\left(\frac{\partial^2 \widetilde{\phi}}{\partial x^2} + \frac{\partial^2 \widetilde{\phi}}{\partial y^2}\right)
\end{aligned}
\tag{17}
$$

where v_b is the artificial turbulence viscosity. The v_b parameter has a recommended value of 1.86 for offshore deep-water wave conditions and 0.0055 for shallow-water waves (Wang et al., 2022). v_b has been calibrated for FNPF with comparisons to model data and CFD simulations.

2.3.3 Coastline algorithm

Creating an efficient grid near the coastline whilst keeping numerical stability when applying a potential flow algorithm near the coastline is difficult. REEF3D::FNPF has its own coastline algorithm to address these issues (Wang et al., 2021).

The coastline algorithm firstly assigns all the cells in the domain as either wet or dry cells given the local water depth h being smaller or larger than a given value $\widehat{h}$. The default threshold $\widehat{h}$ is set to 0.0005 though it may be customised.

$$h = \eta + d \tag{18}$$

$$
\begin{cases}
u = 0, & \text{if } h < \widehat{h} \\
v = 0, & \text{if } h < \widehat{h}
\end{cases}
\tag{19}
$$

After the identification, the wet and dry cells are assigned a value of +1 and -1 respectively, and the velocities in the cells are set to be zero. With the values assigned, the coastline is captured using a two-dimensional level-set function (Osher and Sethian, 1988):

$$
\phi(\vec{x}, t)
\begin{cases}
> 0 \text{ if } \vec{x} \in \text{ wet cell} \\
= 0 \text{ if } \vec{x} \in \Gamma \\
< 0 \text{ if } \vec{x} \in \text{ dry cell}
\end{cases}
\tag{20}
$$

Γ indicates the coastline, and the Eikonal equation $|\nabla\phi| = 1$ holds true in the level-set function. The level-set method is also used to calculate the distance normal to the coastline. The signed distance property of the level-set function must be maintained to ensure mass conservation as the interfaces evolve. Therefore, a reinitialisation process is needed after every time step to calculate the distance to the coastline. REEF3D::FNPF uses a Partial Differential Equation (PDE) based reinitialisation procedure (Sussman, 1994).

$$\frac{\partial \phi}{\partial t} + S(\phi) \left(\left| \frac{\partial \phi}{\partial x_j} \right| - 1 \right) = 0 \tag{21}$$

where $S(\phi)$ is the smooth signed function.

$$S(\phi) = \frac{\phi}{\sqrt{\phi^2 + \left| \frac{\partial \phi}{\partial x_j} \right|^2 (\Delta x)^2}} \tag{22}$$

By using this level-set method, the computational grid remains the same with changes in topography. This gives the model great flexibility, as there is no need to generate a new grid for changes in the topography. Along the wet side of the coastline, relaxation zones are applied. This ensures numerical stability and avoids extreme run-ups. In addition, the reflection of the coastline can be adjusted, which is of great importance when modelling close to harbour areas where there is a varying degree of reflection from natural and artificial obstructions such as breakwaters.

3 SWAN Spectral modeling

3.1 Multi-step simulation using nested grids

The spectral model SWAN is used for the large offshore region around the area of interest due to the high computational efficiency. The simulation is performed in a two-step nested approach. The first step is used for a larger domain with a relatively large cell size, shown as a blue box in Fig. 4 and the second step is a smaller domain with finer cells, shown as a yellow box in Fig. 4. The wave information from the large domain is transferred to the smaller domain in a nested grid.
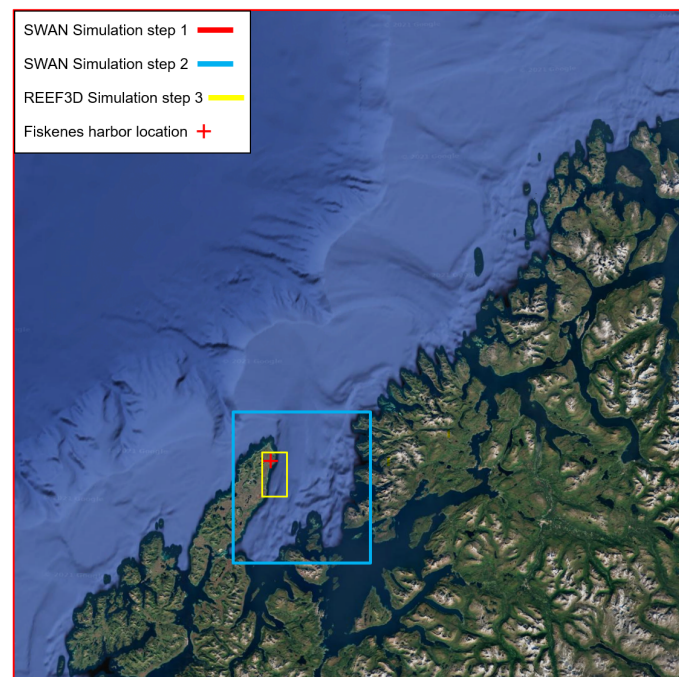

Figure 4: Simulation domains of the multi-step cascade simulation approach.

The bathymetry data is obtained from the Norwegian public source Kartverket (Kartverket, 2021) as well as from the EU initiative EMODnet (EMODnet, 2021) in areas bathymetry data was not available from Kartverket. The bathymetry is shown in Fig. 5a and Fig. 5b for step 1 and step 2 simulations. The bathymetry data for all the simulation steps are in reference to the Universal Transverse Mercator coordinate system (UTM), zone 33N.

In the step 1 simulation, the computational domain has 500 cells in both x and y directions, resulting in a cell size of approximately 450 m, see Table 2. In simulation step 2, the smaller domain is also divided into a 500×500 grid, resulting in cell sizes of approximately 100×100 m, see Table 2. The resulting wave information from simulation step 1 is used as an input into step 2 by using a nested approach at the boundaries, as shown in Fig. 4. A total of seven
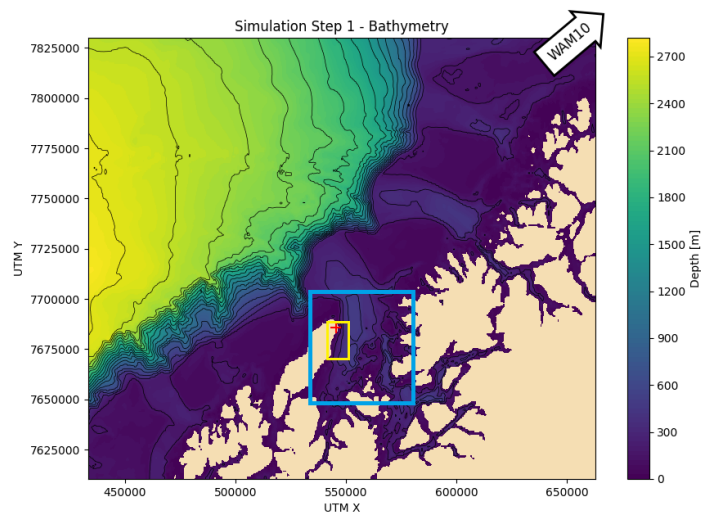
(a) SWAN simulation domain step 1
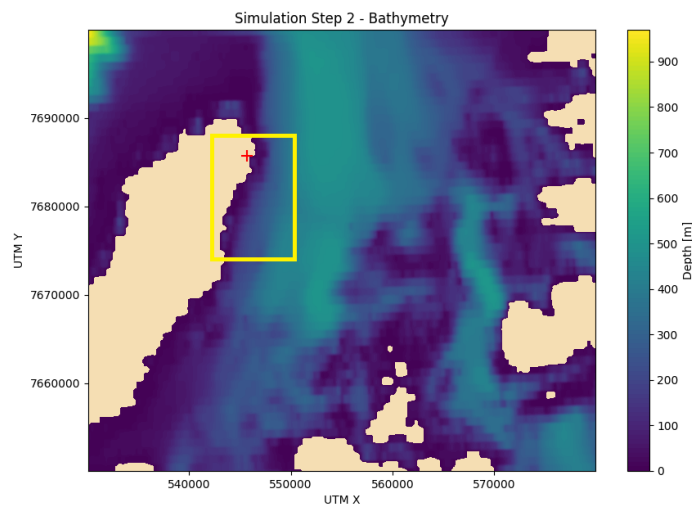
(b) SWAN simulation domain step 2

Figure 5: Bathymetry in the SWAN model for step 1 and step 2 simulations. The offshore hind-cast measurement point is indicated at the upper right corner of (a). The blue box shows the nested domain in the phase-averaging simulations, the yellow box shows the phase-resolving simulation domain.

simulations are performed, one for each hind-cast scenario listed in Table. 1. The standard JONSWAP spectrum from DNV (DNV, 2011) with a peak enhancement factor of 3.3 is used in all simulations. The default $cos^m(\theta)$-type directional spreading function in SWAN is used, with $m = 2$. The input waves are imposed on both the north and west boundaries.

SWAN Simulation	X-extent [m]	Y-extent [m]	cell dx [m]	cell dy [m]
Step 1	229450	219700	458.9	439.4
Step 2	49875	49875	99.8	99.8

Table 2: SWAN simulation cell sizes

At the nesting boundaries, 2000 unique directional spectrums were extracted from the step 1 simulations and serves as the input for the step 2 simulation, i.e. one unique directional spectrum per cell along the boundary. The effect of the nested approach can be seen in Fig. 6, where the significant wave height at the boundary of simulation step 2 is clearly non-homogeneous.
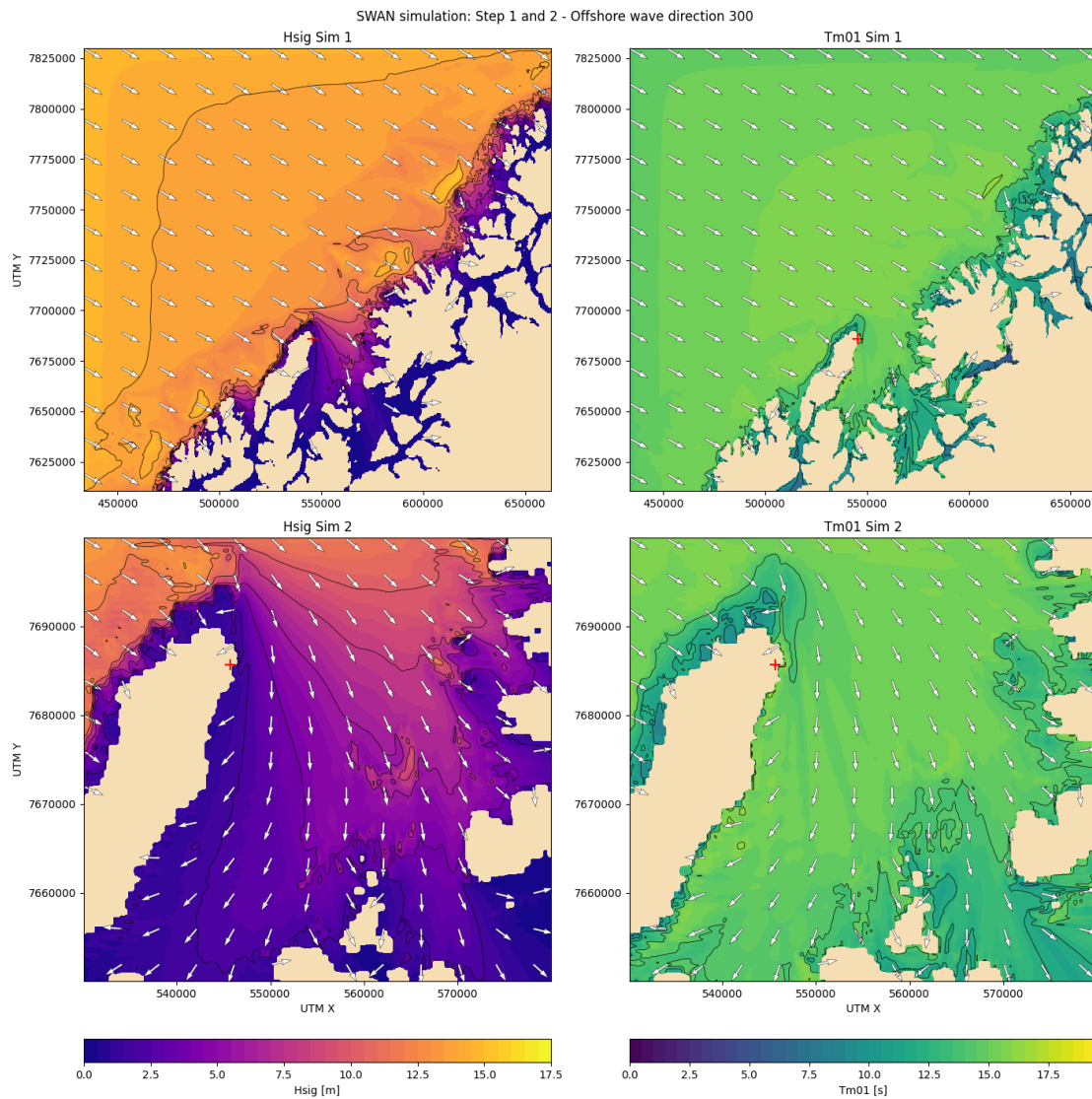

Figure 6: Significant wave height, peak period and mean direction for SWAN simulation Step 1 and 2 for offshore wave direction 300°

3.2 Fast multi-scenario analysis by means of simulation interpolation

It is very inefficient to run simulations for all possible offshore wave directions, which will lead to hundreds of simulations, demanding much computational resource and time. A faster approach is proposed in this study to speed up the multi-scenario analysis process. The simulations were only performed for every 30 degree offshore wave direction between 240 and 90 degrees, as shown in Table 1. Then, the scenarios with offshore principal wave directions in between simulation intervals are interpolated using the simulated results.

Significant wave height (H_s), peak period (T_p), and mean direction (θ_{mean}) for each cell in the simulated domain are extracted for each simulated case. These parameters are used for the missing offshore wave directions by interpolating between the simulations on a cell-by-cell basis. A cubic spline method is used for the interpolation, which ensures a stable solution suitable for interpolating wave states without the oscillations that commonly occur when interpolating with higher-order polynomials (Pollock, 1999). This process is outlined in Fig. 7 and shown in Fig. 8.
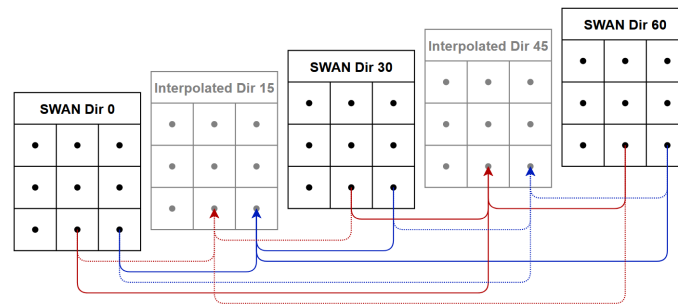

Figure 7: Simplified conceptual interpolation of 3x3 cell domain
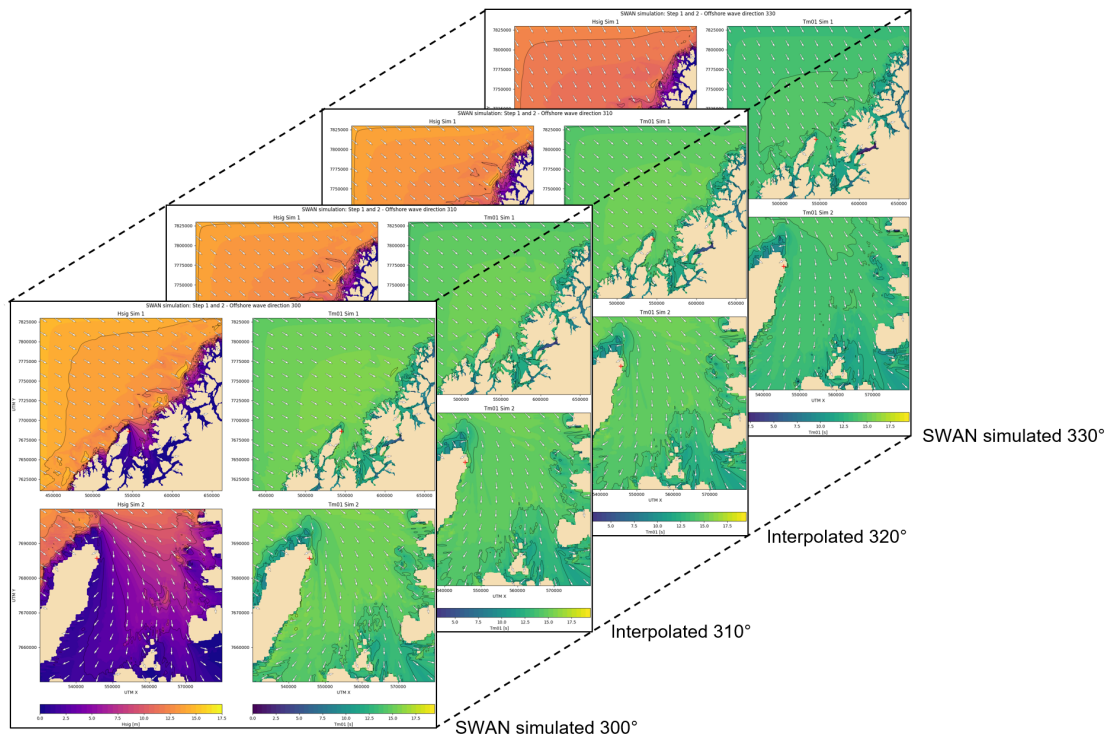
Figure 8: Interpolated sea-states in SWAN simulation

To verify the interpolated results, three additional runs are computed in SWAN with arbitrary offshore wave directions. The verification wave parameters are estimated from the hind-cast data, Table 1, and gives the input for the verification simulations, Table 3.

The mean absolute error, defined in Eqn. 23, is used to determine the accuracy of the interpolation approach for the three main parameters, significant wave height, peak period, and mean direction, as seen in Table 4.

Mean direction	Significant wave height, Hsig	Peak period, Tp
281	16.36	17.63
18	11.08	14.0
36	10.86	14.0

Table 3: Wave parameters verification case in SWAN

$$\text{MAE} = \frac{\sum_{i=1}^{n} |y_i - x_i|}{n} = \frac{\sum_{i=1}^{n} |e_i|}{n} \tag{23}$$

where MAE is the mean absolute error, x_i is the simulated value, y_i is the interpolated value, e_i is the error for cell i, and n is the number of cells in the domain.

SWAN Simulation domain	Domain 1			Domain 2			Average
Offshore wave direction	281	18	36	281	18	36	
Significant wave height - MAE [%]	0.41	2.54	0.67	1.08	0.82	0.29	0.97
Peak period - MAE [%]	0.71	0.58	0.51	0.53	0.31	0.41	0.51
Mean direction - MAE [%]	0.07	11.34	1.39	0.64	4.00	1.64	3.18

Table 4: Mean error difference between SWAN simulated and interpolated in the entire domain.

SWAN Simulation domain	Domain 1			Domain 2			Average
Offshore wave direction	281	18	36	281	18	36	
Significant wave height - MAE [%]	3.84	1.04	1.09	4.19	1.08	1.08	2.05
Peak period - MAE [%]	0.39	0.14	0.08	0.22	0.11	0.00	0.16
Mean direction - MAE [%]	3.20	0.12	0.35	6.75	0.15	0.01	1.76

Table 5: Mean error difference between SWAN simulated and interpolated at the REEF3D input boundary.

It is seen that the average error for the significant wave height and peak period are below 1%, while the error for the mean direction is up to 3.18%. The interpolated results prove to be sufficiently accurate based on the chosen test cases. At the REEF3D simulation boundary, higher errors are observed for waves coming from the western sphere where the diffraction is strong at the northern tip of the island. However, the average errors are still generally bounded within 5%. Though there exist minor errors, the major advantage of the interpolation approach is the computational efficiency. The computational time needed for SWAN simulation and the Python interpolation script is compared in Table 6. The Python script is able to interpolate 210 offshore wave directions with 1.82 percent of the processor time required for just one SWAN simulation. In another word, computing all offshore wave directions in SWAN, with one degree of accuracy, would take 11 554 times more CPU time than cubic spline interpolation of all the cells in Python. However, it is also noted that the largest errors are found at 18 degree angle, which is the furthest away from the actual SWAN simulation angles with a 30-degree interval as it is right in between 0 and 30 degrees. Therefore, there might be more accumulated interpolation error at this angle. Thus the method can benefit from future endeavours on finding a more optimised interpolation scheme.

	SWAN Simulation (1 Offshore wave direction)	Python Interpolation (210 Offshore wave directions)
Real time	291.3 sec	30.9 sec
CPU seconds	1149.9 sec	20.9 sec

Table 6: Comparison simulation time for one SWAN simulation and 210 interpolated offshore wave directions

4   REEF3D::FNPF Phase-resolved modeling

For the final model step, additional bathymetry measurements conducted by Secora AS (dated 12.07.19) near Fiskenes is used. This new bathymetry data set is used in conjunction with the aforementioned bathymetry data obtained from public sources to increase the resolution of the bathymetry, see Fig. 9. The domain length of the numerical wave tank (NWT) in the north-south direction is chosen so that the relevant coastlines that influence wave transformation around the two harbours are included in the domain. The west-east domain length is chosen so that the relevant bathymetric features are included in the domain, such as the deep to shallow water transition. The exact extends in both directions are also limited by the size of the higher resolution bathymetry data from Secora AS. The bathymetry data is rotated in the REEF3D numerical wave tank so that the positive x-direction aligns with the incoming wave direction.
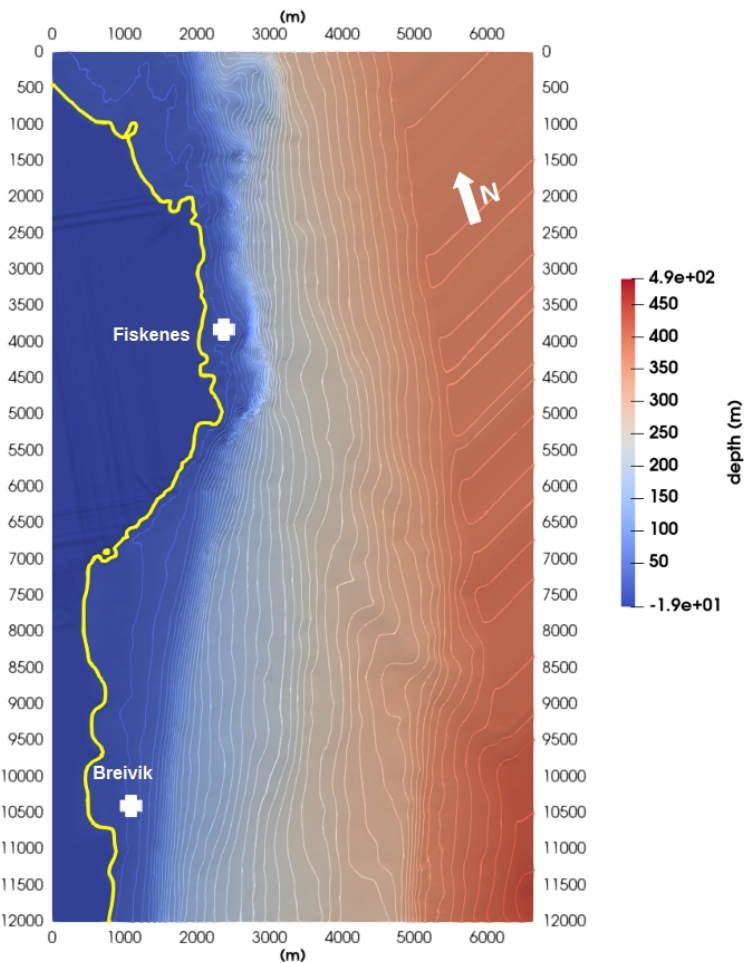

Figure 9: Bathymetry of REEF3D simulation. '+' markers indicate the positions of the principal wave gauges. The yellow curve shows the coastline.

The most extreme wave conditions identified from the SWAN simulations is further investigated using the phase-resolving model. First, the offshore wave direction that is most likely to cause large waves is to be determined. As can be seen from Table 3, the 18° offshore waves have the highest steepness. Therefore, the SWAN simulations have been performed with the 18° offshore waves. The resulting significant wave height, peak period, and mean wave directions at the evenly-spaced wave gauges (with the same spatial interval as the grid resolution in SWAN) located along the north, east and south boundaries of the REEF3D::FNPF domain are obtained from the phase-averaging SWAN simulations. These values are summarised in Fig. 10. It's seen that the highest waves come from the North-East direction.

Therefore, the wave information from SWAN simulation at the North-East corner of the phase-resolving computational domain is plotted in Fig. 11. It is observed that the largest and steepest waves come from the directions between 330° and 40°. Within the North-East section, 30° is seen to lead to the steepest waves and thus chosen to
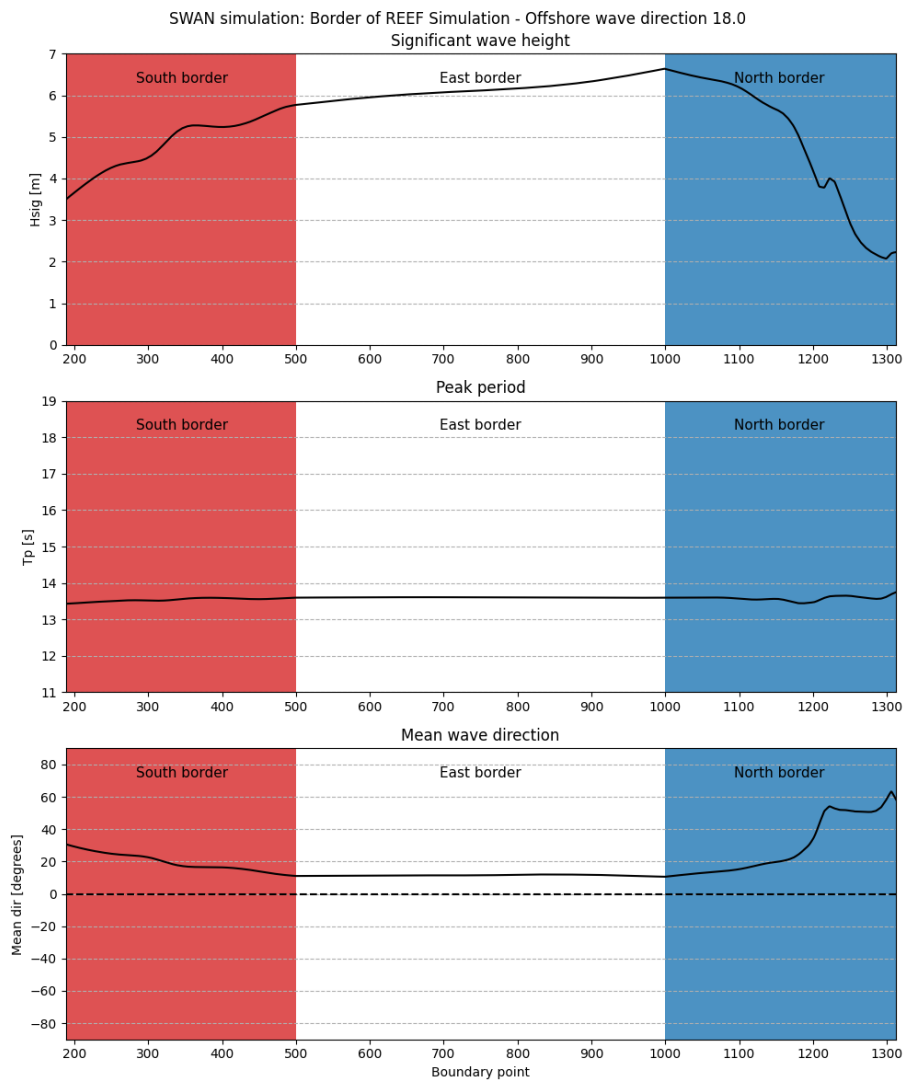
Figure 10: SWAN wave parameters along the boundary of the REEF3D simulation

be the study focus. In addition, 18° is the only hind-cast offshore wave direction that is within the range between 330° and 40°, hence, 18° direction is also identified as a scenario of significance. The resulting input wave scenarios for the phase-resolving model are listed in Table 7. These input waves are imposed at the entire inlet boundary in the FNPF numerical wave tank (NWT). The input spectrum in the phase-resolving model is the JONSWAP with a peak enhancement factor of 3.3. The four distinct wave scenarios for the phase-resolving models are summarised in Table 7.
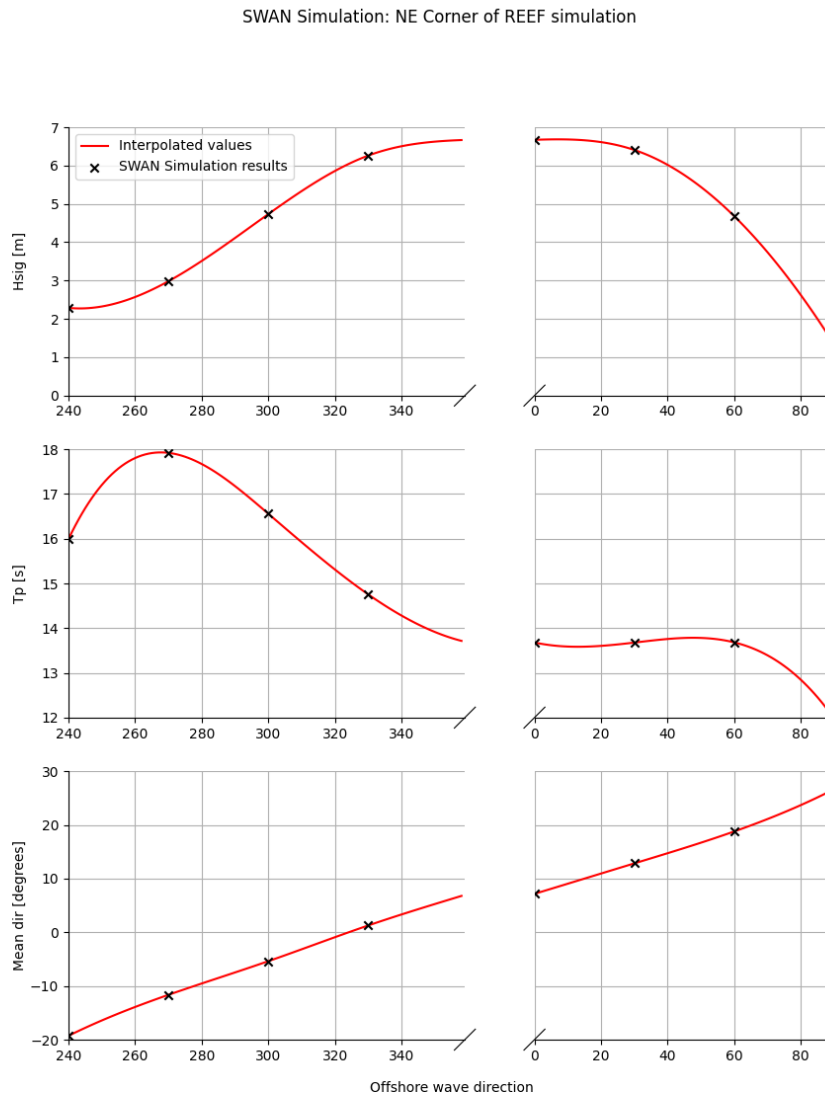

Figure 11: Significant wave height, peak period and mean direction values from SWAN simulation from the northeast corner of REEF3D simulation

SWAN Simulation Offshore direction	REEF3D Simulation	Significant wave height	Peak period	Mean direction	Directional spreading
18	Sim 1	6.67 m	13.7 s	10.7°	ON
30	Sim 2	6.41 m	13.7 s	12.8°	ON
30	Sim 3	6.41 m	13.7 s	12.8°	OFF
30	Sim 4*	6.41 m*	13.7 s	12.8°	OFF
	*Sim 4 uses regular wave with H of 6.41 m				

Table 7: Wave parameters for input uni-directional input spectrums in REEF3D

The horizontal grid size of 10 m is used in the simulations, ensuring 30 cells per wavelength of the peak period, which is usually found sufficient for mild steepness surface wave simulations (Bihs et al., 2020a; Wang et al., 2022). Ten σ-grid notes are arranged in the vertical direction with a clustering factor of 2.5, which was a typical configuration for deep water waves based on the reports of Bihs et al. (2020a) and Wang et al. (2022). A total 8.2 million cells in the hydrodynamic computational domain is used as a result.

In order to generate a map of the significant wave height and the peak period wave gauges were set in a 70x70 grid in the simulation domain for a total of 4900 wave gauges (the upper limit of the number of lines in control files is 5000). After the REEF3D simulation was completed, the time domain analysis was conducted on all the wave gauges. The first 2000 seconds of the analysis were removed to let the sea-state fully develop before the fast Fourier transform (FFT) analysis was run using the rest 3-hour free surface elevation time series.

In addition to the numerical wave gauges needed to generate the significant wave height map, additional wave gauges were set up at some critical locations in the adjacency of each harbour, especially upstream of the wave propagation direction meaning North and North-East of the original wave gauge. The UTM location of each wave gauge in addition to their relative location to the two original wave gauge locations in Fiskenes and Breivik can be seen in Table 8 and shown in Fig. 12.

REEF3D Wave gauge	UTM 33N X [m]	UTM 33N Y [m]	dx [m]	dy[m]
WG1 Fiskenes	546655	7685293	+0	+0
WG2 Fiskenes	546755	7685293	+100	+0
WG3 Fiskenes	546855	7685293	+200	+0
WG4 Fiskenes	546755	7685393	+100	+100
WG5 Fiskenes	546855	7685493	+200	+200
WG6 Fiskenes	547155	7685793	+500	+500
WG7 Breivik	544391	7678434	+0	+0
WG8 Breivik	544591	7678434	+200	+0
WG9 Breivik	544491	7678434	+100	+0
WG10 Breivik	544491	7678534	+100	+100
WG11 Breivik	544591	7678634	+200	+200
WG12 Breivik	544891	7678934	+500	+500

Table 8: Overview of the numerical wave gauges UTM location to access the wave conditions in Fiskenes and Breivik and their offsets from the principal wave gauges closest to the harbour.
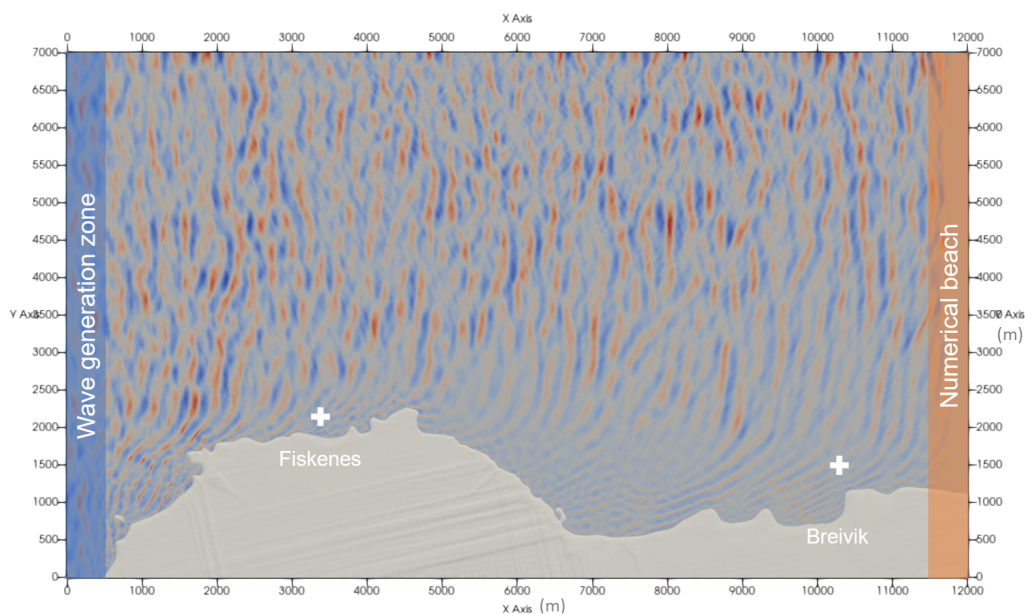

Figure 12: Numerical wave tank configuration in the REEF3D simulations. The wave generation zone is located at the left-hand side boundary and the numerical beach is at the right-hand outlet boundary. The wave gauges for the evaluation of the two sites are marked with white cross. The dimensions of the domain are in meters.

Due to the phase-resolving nature of REEF3D::FNPF, one is able to visualise the free surface in the time-domain. The ability to reconstruct the free surface is advantageous as it gives information about wave physics not possible with phase-averaged models. The free surface at 10 000 seconds simulation time with different principal wave directions can be seen in Fig. 13 and Fig. 14. The significant wave heights at all wave gauges are computed and mapped in Fig. 15a to Fig. 16b.

In the short-crested wave simulations, simulations 1 and 2, the wave fields are relatively homogenous in the far field away from the harbour, as can be assessed from both the free surface elevations in Fig. 13 and the H_s distribution in Fig. 15a and Fig. 15b. As the waves approach the coast, strong shoaling, refraction and diffraction take place as water depth becomes smaller and shoreline affects the wave field. Significant waves are able to propagate into the sheltered region. Longer waves have a stronger capability to bypass obstacles and show stronger diffraction patterns. As a result, long-period waves form a long-crested wave field in the diffraction zone, as seen between the two chosen sites in Fig. 15a. Though wave energy decrease after the diffraction, higher waves are present in the sheltered area than the unidirectional wave simulations, simulation 3 and 4, when one compares Fig. 15a and Fig. 15b with Fig. 16a and Fig. 16b. It seems that the harbours will have higher waves with short-crested wave condition than long-crested wave condition. This highlights the importance of directional spreading and its impact on coastal wave distributions.

In the long-crested irregular waves simulation 3, the wave energy is concentrated in one direction, strong diffraction takes place near Fisknes and Breivik is seen to be better sheltered with smaller waves near the harbour. Right outside the harbours, a stripe of high waves is observed, which is especially visible in the H_s distribution plot in Fig. 16a. This high wave field might be caused by the superposition between the incoming wave and the refracted and diffracted waves. This interaction between the different wave systems has also created higher waves near the upper right boundary. In this scenario, the transport vessels might experience high waves in spite of calmer sea state near the harbours.

The 2nd-order Stokes regular wave in simulation 4 shows a standing wave pattern over the computational domain. A similar interaction between the incoming and transformed wave systems is observed here as in simulation 3. Thus a high wave energy field is observed outside the harbours and downstream from Fiskenes. This wave field then reflect from the side boundary and the outlet numerical beach, creating the standing waves in both the longitudinal and lateral directions. It is noteworthy that regular waves concentrate all wave energy in one direction, one frequency and one phase, thus shows the strongest interactions with the boundaries. Though such regular waves rarely take place in nature, it is important to arrange more dissipative boundaries of large dimensions to fully absorb the wave energy when regular wave is investigated.
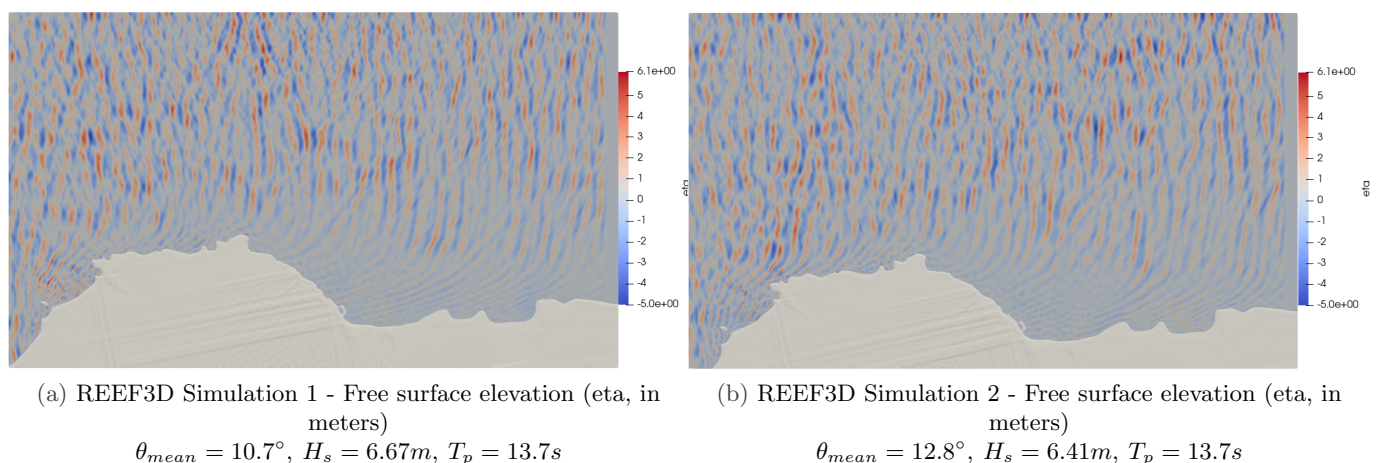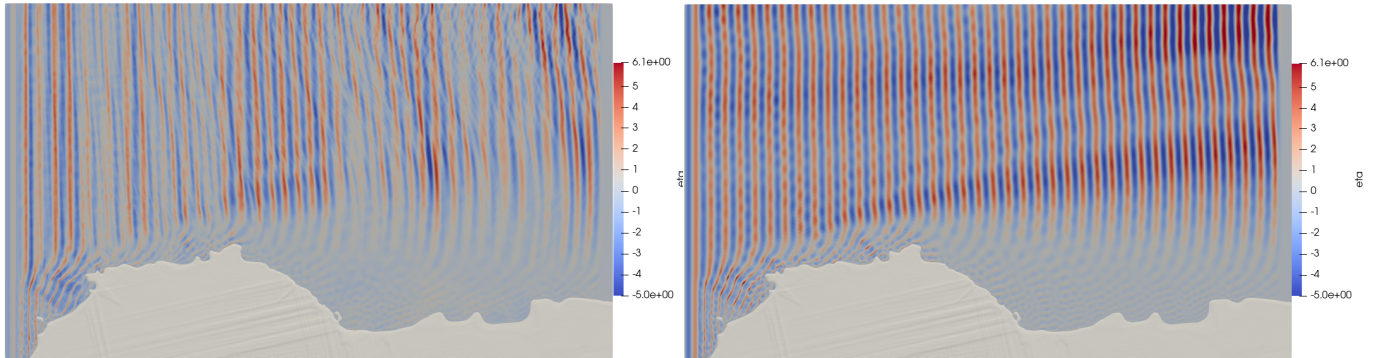

(a) REEF3D Simulation 1 - Free surface elevation (eta, in meters)
$\theta_{mean} = 10.7°$, $H_s = 6.67m$, $T_p = 13.7s$

(b) REEF3D Simulation 2 - Free surface elevation (eta, in meters)
$\theta_{mean} = 12.8°$, $H_s = 6.41m$, $T_p = 13.7s$

Figure 13: REEF3D Simulations free surface elevation visualized in Paraview

The H_s at the critical wave gauges are listed in Table 9 for all four simulations. It's seen that Breivik has generally lower waves, especially under unidirectional wave conditions. The regular wave field shows a very inhomogeneous property due to the standing wave pattern, while the contour of the H_s distribution in Fig. 15a to Fig. 16a gives an overview of the sea states in the adjacency of the harbours. Though Sim 1 has a larger input wave height, Sim 2 shows higher waves near the harbours. This is likely due to the different incident wave angles - the harbours are more exposed to the 30 degree angle from Sim 2. Sim 3 also shows lower waves than Sim 2 near the harbour, which is mostly because the directional spreading in Sim2 propagates more wave energy around the obstacles towards the harbours. The contrast among Sim 1, Sim 2 and Sim 3 further demonstrates the importance of directionality and directional spreading.

(a) REEF3D Simulation 3 - Free surface elevation (eta, in meters)
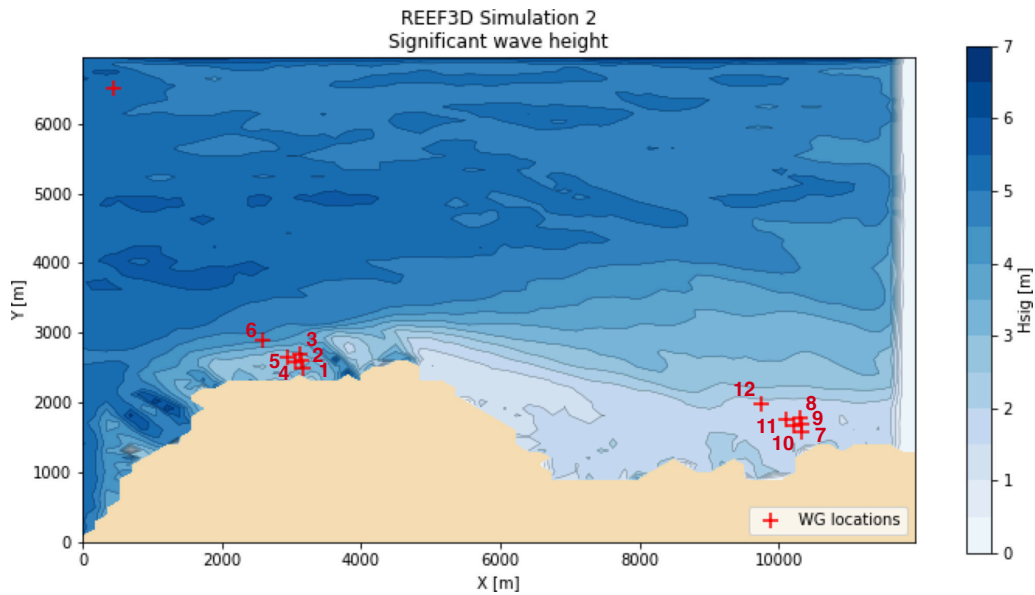$\theta = 12.8°$, $H_s = 6.41m$, $T_p = 13.7s$

(b) REEF3D Simulation 4 - Free surface elevation (eta, in meters)
$\theta = 12.8°$, $H = 6.41m$, $T_p = 13.7s$

Figure 14: REEF3D Simulations free surface elevation visualized in Paraview

REEF3D Simulation		Sim 1	Sim 2	Sim 3	Sim 4
Wave gauge #	Depth [m]	H_s [m]	H_s [m]	H_s [m]	H_{mean} [m]
WG1 Fiskenes	12.4	2.62	2.90	2.41	0.95
WG2 Fiskenes	18.2	2.69	3.01	2.55	1.11
WG3 Fiskenes	30.9	2.99	3.23	2.88	3.31
WG4 Fiskenes	19.8	2.72	2.87	2.52	1.53
WG5 Fiskenes	35.6	2.63	2.89	2.46	1.79
WG6 Fiskenes	147.8	4.16	4.46	5.25	4.02
WG7 Breivik	15.4	1.60	1.74	0.70	0.76
WG8 Breivik	28.8	1.67	1.74	0.67	0.59
WG9 Breivik	21.2	1.61	1.73	0.68	0.85
WG10 Breivik	19.6	1.60	1.68	0.68	0.80
WG11 Breivik	25.5	1.64	1.76	0.65	1.10
WG12 Breivik	53.3	1.79	1.98	0.68	0.79

Table 9: Significant wave height at wave gauges from the REEF3D::FNPF simulation cases and the water depth at the wave gauges
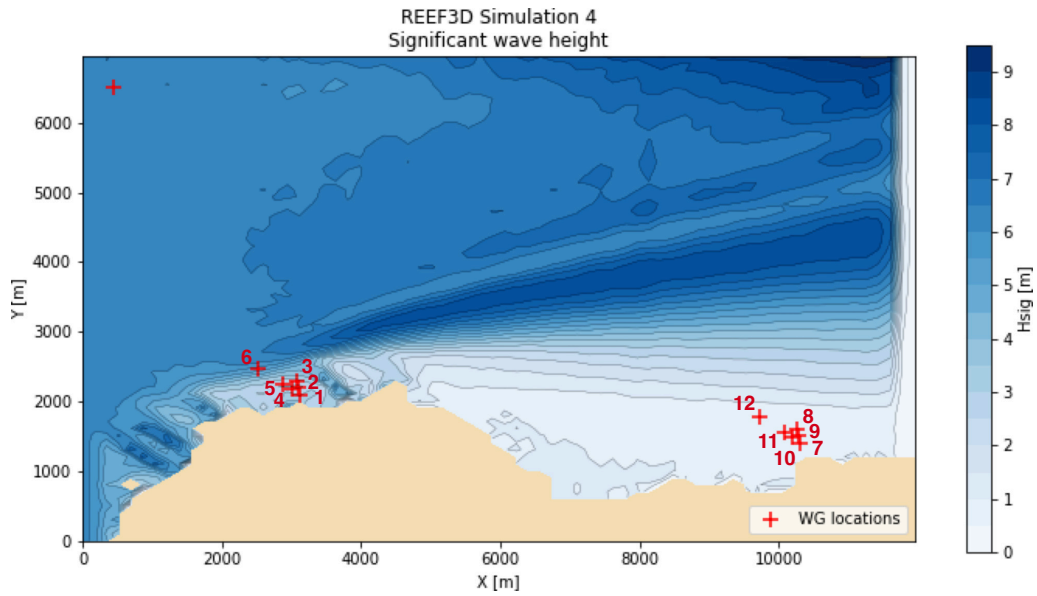
(a) REEF3D Simulation 1 - Significant wave height
$\theta_{mean} = 10.7°$, $H_s = 6.67m$, $T_p = 13.7s$
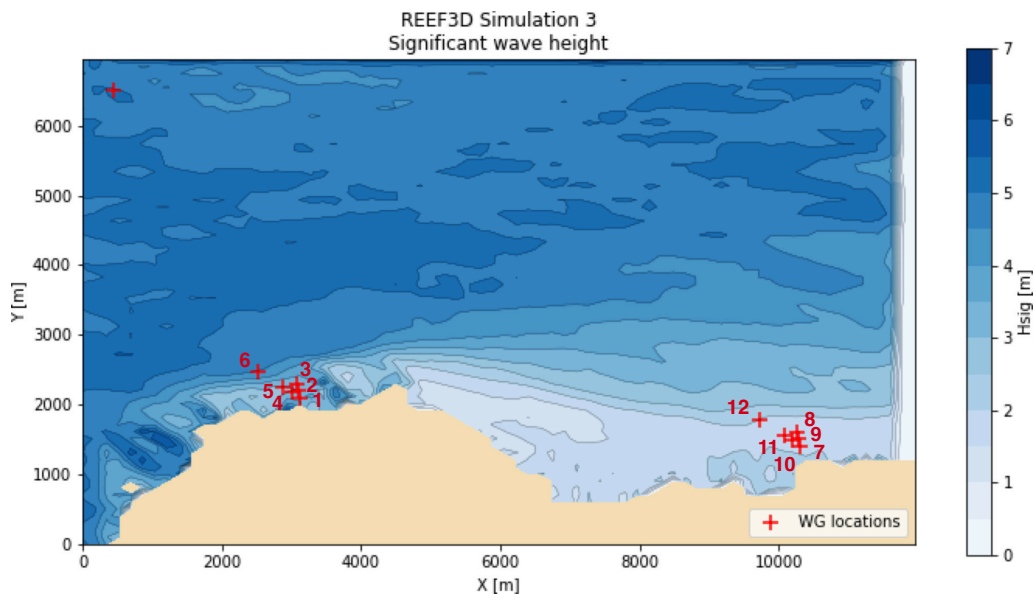
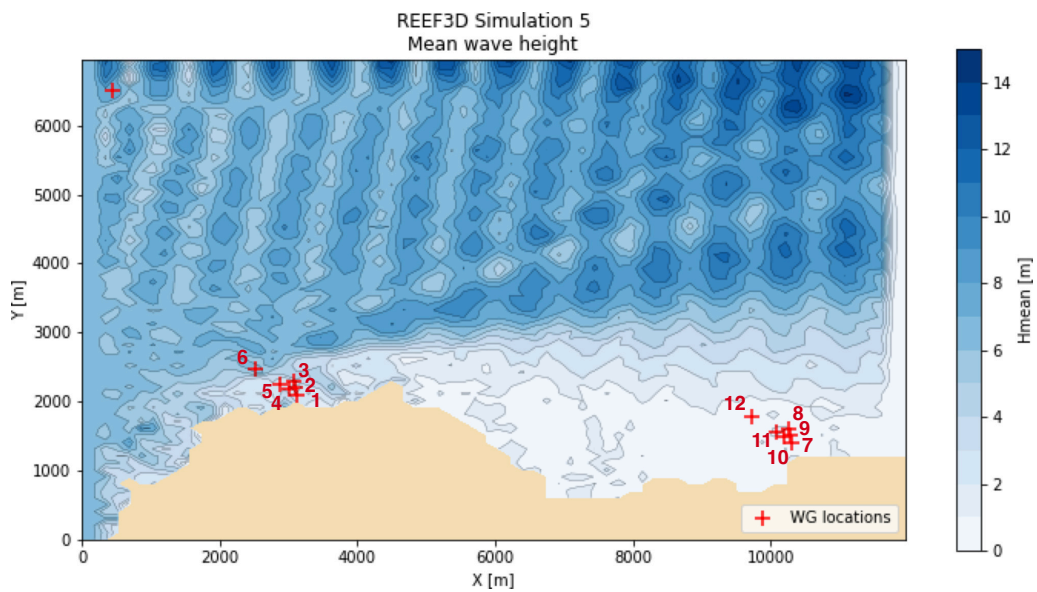(b) REEF3D Simulation 2 - Significant wave height
$\theta_{mean} = 12.8°$, $H_s = 6.41m$, $T_p = 13.7s$

Figure 15: H_s map from REEF3D simulations 1 and 2

(a) REEF3D Simulation 3 - Significant wave height
$\theta = 12.8°$, $H_s = 6.41m$, $T_p = 13.7s$

(b) REEF3D Simulation 4 - Mean wave height
$\theta = 12.8°$, $H = 6.41m$, $T_p = 13.7s$

Figure 16: H_s and H_{mean} map from REEF3D simulations 3 and 4

The REEF3D::FNPF simulations ran on the supercomputer Fram with 256 cores for approximately 15 hours, the CPU usage is outlined in Table 10. As reported by Wang et al. (2020a), the FNPF model is typically in the order of 1000 times faster than a typical Navier-Stokes solver. It indicates a more than 600 days simulation if a Navier-Stokes solver is to be applied using a similar computational infrastructure, which is practically not acceptable for design purposes. It's seen that the irregular wave simulations are generally slightly slower than the regular wave simulation but not by a large margin.

REEF3D Simulation	CPU cores	Simulation time (h)
Sim 1	256	14:57:14
Sim 2	256	15:38:23
Sim 3	256	16:38:35
Sim 4	256	14:09:32

Table 10: Overview of computational time for the 3-hour REEF3D simulations.

5   Conclusions

A combined phase-averaging and phase-resolving numerical modelling approach has been deployed to analyse the wave environment at a Norwegian coast for onshore aquaculture harbour assessment. The open-source phase-averaging spectrum wave model SWAN is used for the large-domain offshore wave analysis based on the offshore measurements. A nested grid approach is used to acquire high-resolution results near the area of interest with a low computational cost.

A novel interpolation scheme is used to obtain sea state at every offshore wave directions and provide comprehensive overviews that facilitate a much faster extreme event identification. The approach is about 10000 time faster than running simulations for each direction. A severe sea state near the area of interest is identified from the north-east boundary and used as the input for the phase-resolving model where wave diffraction due to the coastline is significant. However, to conclude on the most severe case at the harbours, further developments to include variable boundaries in the phase-resolving model and the 3D effects from the phase-averaging wave field are needed.

The open-source fully nonlinear potential flow model REE3D::FNPF is employed, where both breaking algorithm and coastline algorithm ensure robust coastal wave transformation simulations. Four characteristic scenarios are simulated and an array of wave gauges evenly spaced in the entire computational domain are arranged to obtain the significant wave height distribution. This way, the phase-resolving simulations present the wave energy distribution in a similar manner as a phase-averaging model but with more resolved information where diffraction is significant. The simulations in the current study for the 12km × 6km domain take only around 15 hours. Combined with the interpolation algorithm in the SWAN simulation, the hybrid approach provides a significant speed boost for the large-scale multi-scenario sea state assessment.

Both candidate locations, Breivik and Fiskenes, show strong wave transformations. Breivik has generally smaller waves in the presented scenario. The combined numerical approach proves to be computationally efficient and combine the advantages of both the phase-averaging models and the phase-resolving models for the sea state analysis of a large area under a large number of scenarios. The procedure and technique can be extended to various applications with different scales and coastal topography.

In the future, a more integrated flow information exchange between the phase-averaging model and the phase-resolving model in a form of an application interface (API) shall be explored for a better coupling between the models. The capability of reading in a directional spectrum from the phase-averaging model should be implemented in the phase-resolving model. A segmented wave generation boundary in the phase-resolving model is also expected for flexible inhomogeneous wave generations by using multiple spectra from the phase-averaging model. For the phase-averaging model studies, wind-generated waves should be included in the future, and a more optimised interpolation scheme should be further explored for improved accuracy and efficiency.

Acknowledgements

titled 'Wave environment assessment at a Norwegian harbour for land-based aquaculture facilities using a combined numerical approach'. The simulations were performed on the supercomputer Fram provided by UNINETT Sigma2 - the National Infrastructure for High-Performance Computing and Data Storage in Norway.

Author contributions (CRediT)

Knut Reidulff : Data curation, Formal Analysis, Investigation, Simulation, Writing-original draft. Weizhi Wang: Conceptualisation, Methodology, Supervision, Simulation, Writing-original draft, Writing-review & editing. Arun Kamath: Methodology, Resources, Supervision. Hans Bihs: Conceptualisation, Methodology, Resources, Software, Supervision

Notations

Name	Symbol	Unit
Acceleration due to gravity	g	m/s^2
Sigma coordinate	σ	...
Velocity potential	Φ	m^2/s
Particle velocities in x, y z direction	u, v, w	m/s
Vertical grid starching factor	α	...
Free surface elevation	η	m
Added viscosity	ν_b	m^2/s
Local water depth	h	m^2/s
Still water depth	d	m^2/s
Wetting-drying criterion	$\widehat{h}$	m^2/s
Level-set function	ϕ	m^2/s
Wave variance density	E	m^2/Hz
Wave action density	N	$m^2 s^2$
Frequency	f	Hz
Relative frequency	f_σ	Hz
Wave direction	θ	$^\circ$
Source term in wave action balance equation	S	...
Significant wave height	H_s	m
Peak period	T_p	s

References

Ahmad, N., Kamath, A. and Bihs, H. (2020). 3D numerical modelling of scour around a jacket structure with dynamic free surface capturing. *Ocean Engineering*, **200**, 107104. ISSN 00298018. DOI:10.1016/j.oceaneng.2020.107104.

Alagan Chella, M., Bihs, H. and Myrhaug, D. (2019). Wave impact pressure and kinematics due to breaking wave impingement on a monopile. *Journal of Fluids and Structures*, **86**, 94–123. ISSN 10958622. DOI:10.1016/j.jfluidstructs.2019.01.016.

Andfjord Salmon (2021). Andfjord Salmon, https://www.andfjord.no/.

Ardhuin, F. and Roland, A. (2013). The development of spectral wave models: Coastal and coupled aspects, In: *Proceedings of Coastal Dynamics 2013: 7th International Conference on Coastal Dynamics*.

Baquet, A., Kim, J. and Huang, Z. (2017). Numerical modeling using CFD and potential wave theory for three-hour nonlinear irregular wave simulations, In: *Proceedings of the International Conference on Offshore Mechanics and Arctic Engineering - OMAE*, volume 1, American Society of Mechanical Engineers (ASME).

Bihs, H., Kamath, A., Alagan Chella, M., Aggarwal, A. and Arntsen, Ø.A. (2016a). A new level set numerical wave tank with improved density interpolation for complex wave hydrodynamics. *Computers and Fluids*, **140**, 191–208. ISSN 00457930. DOI:10.1016/j.compfluid.2016.09.012.

Bihs, H., Kamath, A., Alagan Chella, M., Aggarwal, A. and Arntsen, Ø.A. (2016b). A new level set numerical wave tank with improved density interpolation for complex wave hydrodynamics. *Computers & Fluids*, **140**(Supplement C), 191 – 208. ISSN 0045-7930. DOI:https://doi.org/10.1016/j.compfluid.2016.09.012.

Bihs, H., Wang, W., Martin, T. and Kamath, A. (2020a). REEF3D::FNPF - A Flexible Fully Nonlinear Potential Flow Solver. *Journal of Offshore Mechanics and Arctic Engineering*.

Bihs, H., Wang, W., Pákozdi, C. and Kamath, A. (2020b). REEF3D::FNPF—A flexible fully nonlinear potential flow solver. *Journal of Offshore Mechanics and Arctic Engineering*, **142**(4), 041902. ISSN 0892-7219. DOI:10.1115/1.4045915.

Bingham, H.B. and Zhang, H. (2007). On the accuracy of finite-difference solutions for nonlinear water waves. *Journal of Engineering Mathematics*, **58**(1), 211–228. ISSN 1573-2703. DOI:10.1007/s10665-006-9108-4.

Bonnefoy, F., Touzé, D.L. and Ferrant, P. (2006a). A fully-spectral 3d time-domain model for second-order simulation of wavetank experiments. part a: Formulation, implementation and numerical properties. *Applied Ocean Research*, **28**(1), 33 – 43. ISSN 0141-1187. DOI:https://doi.org/10.1016/j.apor.2006.05.004.

Bonnefoy, F., Touzé, D.L. and Ferrant, P. (2006b). A fully-spectral 3d time-domain model for second-order simulation of wavetank experiments. part b: Validation, calibration versus experiments and sample applications. *Applied Ocean Research*, **28**(2), 121 – 132. ISSN 0141-1187. DOI:https://doi.org/10.1016/j.apor.2006.05.003.

Booij, N., Ris, R.C. and Holthuijsen, L.H. (1999). A third-generation wave model for coastal regions 1. Model description and validation. *Journal of Geophysical Research: Oceans*, **104**(C4), 7649–7666. ISSN 21699291. DOI:10.1029/98JC02622.

DNV (2011). Modelling and analysis of marine operations, Standard DNV-RP-H103, Det Norske Veritas, Veritasveien 1, Høvik, Norway.

Ducrozet, G., Bonnefoy, F.e.l., Le Touz é, D. and Ferrant, P. (2012). A modified High-Order Spectral method for wavemaker modeling in a numerical wave tank. *European Journal of Mechanics - B/Fluids*, **34**. DOI:10.1016/j.euromechflu.2012.01.017.

EMODnet (2021). EMODnet Bathymetry, https://www.emodnet-bathymetry.eu/.

Engsig-Karup, A., Bingham, H. and Lindberg, O. (2009). An efficient flexible-order model for 3D nonlinear water waves. *Journal of Computational Physics*, **228**, 2100–2118.

Fjørtoft, T. and Fondevik, T. (2020). Land-based salmon farming in Norway – laws and regulations.

Grilli, A.R., Westcott, G., Grilli, S.T., Spaulding, M.L., Shi, F. and Kirby, J.T. (2020). Assessing coastal hazard from extreme storms with a phase resolving wave model: Case study of narragansett, ri, usa. *Coastal Engineering*, **160**, 103735. ISSN 0378-3839. DOI:https://doi.org/10.1016/j.coastaleng.2020.103735.

Grilli, S.T., Subramanya, R., Svendsen, I.A. and Veeramony, J. (1994). Shoaling of solitary waves on plane beaches. *Journal Waterway Port Coastal and Ocean Enigneering*, **120**(6), 609–628.

Jacobsen, N.G., Fuhrman, D.R. and Fredsøe, J. (2012). A wave generation toolbox for the open-source CFD library: OpenFoam®. *International Journal for Numerical Methods in Fluids*, **70**(9), 1073–1088. ISSN 02712091. DOI:10.1002/fld.2726.

Jensen, J.H., Madsen, E.Ø. and Fredsøe, J. (1999). oblique flow over dredged channels. II: Sediment transport and morphology. *Journal of Hydraulic Engineering (Reston)*, **125**(11), 1190–1198. ISSN 0733-9429.

Jeschke, A., Pedersen, G.K., Vater, S. and Behrens, J. (2017). Depth-averaged non-hydrostatic extension for shallow water equations with quadratic vertical pressure profile: equivalence to boussinesq-type equations. *International Journal for Numerical Methods in Fluids*, **84**(10), 569–583. DOI:10.1002/fld.4361.

Jiang, G.S. and Shu, C.W. (1996). Efficient implementation of weighted ENO schemes. *Journal of Computational Physics*, **126**(1), 202–228. ISSN 00219991. DOI:10.1006/jcph.1996.0130.

Kartverket (2021). Kartverket, https://hoydedata.no/LaserInnsyn/.

Li, B. and Fleming, C.A. (1997). A three dimensional multigrid model for fully nonlinear water waves. *Coastal Engineering*, **30**(3), 235 – 258. ISSN 0378-3839. DOI:https://doi.org/10.1016/S0378-3839(96)00046-4.

Madsen, P.A., Bingham, H.B. and Liu, H. (2002). A new Boussinesq method for fully nonlinear waves from shallow to deep water. *Journal of Fluid Mechanics*, **462**, 1–30.

Madsen, P.A., Murray, R. and Sørensen, O.R. (1991). A new form of the Boussinesq equations with improved linear dispersion characteristics. *Coastal Engineering*, **15**, 371–388.

Martin, T., Kamath, A. and Bihs, H. (2020). A Lagrangian approach for the coupled simulation of fixed net structures in a Eulerian fluid model. *Journal of Fluids and Structures*, **94**, 102962. ISSN 10958622. DOI:10.1016/j.jfluidstructs.2020.102962.

Massey, T.C., Anderson, M.E., Smith, J., Gomez, J. and Jones, R. (2011). STWAVE: Steady-State Spectral Wave Model User's Manual for STWAVE, Version 6.0, Technical report, US Army Corps of Engineers, Washington, DC 20314-1000.

Norwegian Building Authority (2017). Regulations om technical requirements for construction works (TEK17), Technical report.

NRK (2022). Vil bygge oppdrettsanlegg like ved flyplass – frykter fuglekrasj og lysforurensing, https://www.nrk.no/nordland/frarader-bygging-av-nytt-oppdrettsanlegg-ved-andoya-lufthavn-1.15993051.

Nwogu, O. (1993). Alternative form of Boussinesq equations for nearshore wave propagation. *Journal of Waterways, Port, Coastal, and Ocean Engineering*, **119**(6), 618–638.

OpenFOAM (2019). OpenFOAM User Guide Version 7, Technical report, The OpenFOAM Foundation.

Osher, S. and Sethian, J.A. (1988). Fronts propagating with curvature-dependent speed: Algorithms based on Hamilton-Jacobi formulations. *Journal of Computational Physics*, **79**(1), 12–49. ISSN 10902716. DOI: 10.1016/0021-9991(88)90002-2.

Pollock, D. (1999). Smoothing with Cubic Splines, In: *Handbook of Time Series Analysis, Signal Processing, and Dynamics*, 293–322, Elsevier.

Raoult, C., Benoit, M. and Yates, M.L. (2016). Validation of a fully nonlinear and dispersive wave model with laboratory non-breaking experiments. *Coastal Engineering*, **114**, 194 – 207. ISSN 0378-3839. DOI:https://doi.org/10.1016/j.coastaleng.2016.04.003.

Reistad, M., Breivik, Ø., Haakenstad, H., Aarnes, O.J. and Furevik, B.R. (2009). A high-resolution hindcast of wind and waves for The North Sea, The Norwegian Sea and The Barents Sea Title A high-resolution hindcast of wind and waves for The North Sea, The Norwegian Sea and The Barents Sea. ISSN 1503-8025.

Shi, F., Kirby, J.T., Harris, J.C., Geiman, J.D. and Grilli, S.T. (2012). A high-order adaptive time-stepping tvd solver for boussinesq modeling of breaking waves and coastal inundation. *Ocean Modelling*, **43-44**, 36 – 51. ISSN 1463-5003. DOI:https://doi.org/10.1016/j.ocemod.2011.12.004.

Shu, C.W. and Osher, S. (1988). Efficient implementation of essentially non-oscillatory shock-capturing schemes. *Journal of Computational Physics*, **77**(2), 439–471. ISSN 10902716. DOI:10.1016/0021-9991(88)90177-5.

Siemens (2019). Simcenter STARCCM+ User Guide, Technical report, Siemens.

Smit, P., Zijlema, M. and Stelling, G. (2013). Depth-induced wave breaking in a non-hydrostatic, near-shore wave model. *Coastal Engineering*, **76**, 1–16. ISSN 03783839. DOI:10.1016/j.coastaleng.2013.01.008.

Stelling, G.S. and Duinmeijer, S.P.A. (2003). A staggered conservative scheme for every froude number in rapidly varied shallow water flows. *International Journal for Numerical Methods in Fluids*, **43**(12), 1329–1354. DOI:10.1002/fld.537.

Sussman, M. (1994). A level set approach for computing solutions to incompressible two-phase flow. *Journal of Computational Physics*, **114**(1), 146–159. ISSN 00219991. DOI:10.1006/jcph.1994.1155.

van der Vorst, H.A. (1992). Bi-CGSTAB: A Fast and Smoothly Converging Variant of Bi-CG for the Solution of Nonsymmetric Linear Systems. *SIAM Journal on Scientific and Statistical Computing*, **13**(2), 631–644. ISSN 0196-5204. DOI:10.1137/0913035.

Vaz, G., Jaouen, F. and Hoekstra, M. (2009). Free-Surface Viscous Flow Computations: Validation of URANS Code FreSCo, volume Volume 5: Polar and Arctic Sciences and Technology; CFD and VIV of *International Conference on Offshore Mechanics and Arctic Engineering*, 425–437.

Wang, W. (2020). Large-Scale Phase-Resolved Wave Modelling for the Norwegian Coast.

Wang, W., Kamath, A., Martin, T., Pákozdi, C. and Bihs, H. (2020*a*). A comparison of different wave modelling techniques in an open-source hydrodynamic framework. *Journal of Marine Science and Engineering*, **8**, 7. ISSN 2077-1312. DOI:10.3390/jmse8070526.

Wang, W., Martin, T., Kamath, A. and Bihs, H. (2020*b*). An improved depth-averaged nonhydrostatic shallow water model with quadratic pressure approximation. *International Journal for Numerical Methods in Fluids*, **92**(8), 803–824. DOI:10.1002/fld.4807.

Wang, W., Pákozdi, C., Kamath, A. and Bihs, H. (2021). A fully nonlinear potential flow wave modelling procedure for simulations of offshore sea states with various wave breaking scenarios. *Applied Ocean Research*, **117**, 102898. ISSN 0141-1187. DOI:https://doi.org/10.1016/j.apor.2021.102898.

Wang, W., Pákozdi, C., Kamath, A., Fouques, S. and Bihs, H. (2022). A flexible fully nonlinear potential flow model for wave propagation over the complex topography of the norwegian coast. *Applied Ocean Research*, **122**, 103103. ISSN 0141-1187. DOI:https://doi.org/10.1016/j.apor.2022.103103.

Yates, M.L. and Benoit, M. (2015). Accuracy and efficiency of two numerical methods of solving the potential flow problem for highly nonlinear and dispersive water waves. *International Journal for Numerical Methods in Fluids*, **77**(10), 616–640. DOI:10.1002/fld.3992.

Zijlema, M. and Stelling, G. (2008). Efficient computation of surf zone waves using the nonlinear shallow water equations with non-hydrostatic pressure. *Coastal Engineering*, **55**(10), 780 – 790. ISSN 0378-3839. DOI:https://doi.org/10.1016/j.coastaleng.2008.02.020.

Zijlema, M., Stelling, G. and Smit, P. (2011). SWASH: An operational public domain code for simulating wave fields and rapidly varied flows in coastal waters. *Coastal Engineering*, **58**(10), 992 – 1012. ISSN 0378-3839. DOI: https://doi.org/10.1016/j.coastaleng.2011.05.015.

Zijlema, M. and Stelling, G.S. (2005). Further experiences with computing non-hydrostatic free-surface flows involving water waves. *International Journal for Numerical Methods in Fluids*, **48**(2), 169–197. DOI:10.1002/fld.821.